Propagation and Scattering in Ducting Maritime Environments From an Accelerated Boundary Integral Equation

Christophe Bourlier

***Abstract*— For a 2-D problem and at microwave radar frequencies, in a previous paper, the field scattered by a highly conducting large rough sea surface in the presence of a duct having a linear-square refractive index profile has been computed. The forward–backward (FB) method has been applied to solve the linear system obtained by discretizing the boundary integral equation from the method of moments. To reduce again the complexity in order to solve huge problems, the subdomain decomposition iterative method is applied and combined with the FB spectral-acceleration for the calculation of the surface currents on each subsurface of the sea. The adaptive cross approximation algorithm is also applied to accelerate the coupling steps between the subsurfaces. Finally, this method is tested on the medium having a refractive index of parabolic profile, which is more realistic than a linear profile.**

***Index Terms*— Adaptive cross approximation (ACA), iterative methods, method of moments (MoMs), parabolic wave equation (PWE), radar sea surface electromagnetic scattering.**

I. Introduction

OCEAN atmospheric ducts are common occurrences in many maritime regions of the world, and the ducts result in significant changes in the propagation characteristics of radio wave and affect the performance of electronic systems, such as shipboard radars and radio communication system. Therefore, it is quite important to research on the propagation characteristics of radio wave in the ocean atmospheric duct environment to improve the efficiency of maritime electronic systems.

Under the conditions of predominant forward propagation and scattering, i.e., when the rough sea surface is gently undulating and the angles of propagation and scattering are grazing, the parabolic wave equation (PWE) approximation combined with split-step Fourier (SSF) gives satisfactory results. For a complete review of this method, see the textbook of Levy [1] and the references therein. The great advantage of the PWE-SSF method is that it can deal with most real-life inhomogeneous environments and is that it fast (based on the calculation of successions of FFTs). Its main drawback is the underlying paraxial approximation leading to an approximation of the propagator (that is, Green's function) and the boundary conditions are determined from a heuristic way, for instance from the Ament reflection coefficient [2], [3].

The well-known method of moments (MoMs) [4]–[6] is a way of solving rigorously the scattering problem by converting the boundary integral equation (BIE) into a linear system, in which the impedance matrix must be inverted to determine the surface currents. Then, the scattered field is computed by radiating the surface currents. For a ducting environment, the main drawback of the MoM is that Green's function (propagator) is known only for a small class of refractive index profiles [7], [8]. That is why, when the BIE method is applied [9]–[13], the propagator is usually derived under the PWE approximation. These references assumed a duct having a linear-square refractive index profile. In [11] and [13], the forward–backward (FB) [15], [16] method is employed to solve the linear system. The advantage of the FB is that only a row of the impedance matrix needs to be stored, instead of the whole matrix from a direct lower upper (LU) decomposition. The drawback is that the elements of the impedance matrix must be recomputed for each FB order, which can be very time consuming.

The purpose of this paper is to overcome this issue by using the recent [14] subdomain decomposition iterative method (SDIM) in order to solve a huge problem and rapidly. In addition, the size of each subdomain of SDIM is chosen such as the domain can be considered as homogeneous (the refractive index is assumed to be a constant) to apply the FB combined with the spectral-acceleration (SA) [17]. Another advantage of the decomposition of the sea surface into subsurfaces is that the duct parameters can change with the range as done from a PWE-SSF scheme. Awadallah *et al.* [12] presented a similar approach but the coupling between the subsurfaces is made via a vertical phase screen by considering only the forward contribution, which is completely different from our approach. SDIM is also combined with the adaptive cross approximation (ACA) algorithm [19], [20] to accelerate all the coupling steps between the subsurfaces. This paper will show that the resulting complexity of the method, named "SDIM + FBSA + ACA," is strongly reduced both in memory requirement and computing time in comparison to a direct LU decomposition of the impedance matrix of the whole surface.

Manuscript received April 4, 2016; revised June 14, 2016; accepted July 25, 2016. Date of publication August 30, 2016; date of current version October 27, 2016.

The author is with the Institut d'Électronique et de Télécommunications de Rennes Laboratory, L'Université Nantes Angers Le Mans, University of Nantes, 44306 Nantes, France (e-mail: christophe.bourlier@univ-nantes.fr).

Color versions of one or more of the figures in this paper are available online at http://ieeexplore.ieee.org.

Digital Object Identifier 10.1109/TAP.2016.2604464

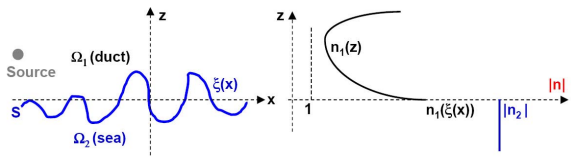

Fig. 1. Left: illustration of the scattering problem, where $\xi(x)$ is the surface elevation versus its abscissa x. Right: profile of the modulus of the refractive index $n(z)$. For $z < \xi(x)$, $n(z) = n_2$ and for $z > \xi(x)$, $n(z) = n_1(z)$.

Finally, this method is tested on a medium having a refractive index of parabolic profile, which is more realistic than a linear profile.

This paper is organized as follows. Section II briefly summarizes the SDIM combined with ACA and FBSA by giving the resulting complexity. Section III derives the Green function under the PWE approximation and Section IV presents numerical results. Section V gives concluding remarks.

II. SDIM Combined With FBSA and ACA

A. Integral Equations

The purpose of this paper is to calculate the field scattered by the rough surface in medium Ω_1 when the source is located in medium Ω_1 (Fig. 1) by accounting for the refraction effect, since the medium Ω_1 is inhomogeneous. A method must be developed to compute the surface currents on the rough surface, then from the knowledge of these surface currents, to calculate the scattered field in Ω_1 from Huygens' principle.

The surface currents S are computed from the BIE method that, in general, requires solving for both the field and its normal derivative. Since the sea surface is highly conductive for microwave frequencies, the impedance (or Leontovich) boundary condition (IBC) can be applied

$$\begin{cases} \text{TE}: \psi(\boldsymbol{r}) = \alpha_{\text{TE}} \dfrac{\partial \psi(\boldsymbol{r})}{\partial n}, & \alpha_{\text{TE}} = \dfrac{j}{k_0} \dfrac{n_1(0^+)}{n_2} \\ \text{TM}: \dfrac{\partial \psi(\boldsymbol{r})}{\partial n} = \alpha_{\text{TM}} \psi(\boldsymbol{r}), & \alpha_{\text{TM}} = \dfrac{k_0}{j} \dfrac{n_1(0^+)}{n_2}. \end{cases} \tag{1}$$

This leads to the following BIE [5], [6] for $\forall (\boldsymbol{r}, \boldsymbol{r}') \in S$:

$$\begin{cases} \text{TE}: \psi_l(\boldsymbol{r}') = \displaystyle\int_S \frac{\partial \psi(\boldsymbol{r})}{\partial n} \left[g(\boldsymbol{r}, \boldsymbol{r}') - \alpha_{\text{TE}} \frac{\partial g(\boldsymbol{r}, \boldsymbol{r}')}{\partial n} \right] dS \\ \text{TM}: \psi_l(\boldsymbol{r}') = \dfrac{1}{2} \psi(\boldsymbol{r}') \\ \qquad\qquad + \displaystyle\int\!\!\!\!\!\!\diagup_S \psi(\boldsymbol{r}) \left[g(\boldsymbol{r}, \boldsymbol{r}') \alpha_{\text{TM}} - \frac{\partial g(\boldsymbol{r}, \boldsymbol{r}')}{\partial n} \right] dS. \end{cases} \tag{2}$$

In addition, n_2 (constant) is the refractive index of medium Ω_2, $n_1(0^+)$ is the refractive index of medium Ω_1 for $z = 0$ (mean plane of the sea rough surface), assumed to be independent of x ($n_1(\xi(x)) \approx n_1(0^+)$), $k_0 = 2\pi/\lambda_0$ (λ_0 being the EM wavelength in free space) is the incident wave number of the source, which is assumed to be located inside Ω_1, ψ_l is the incident field on the surface, g is the spatial Green's function in Ω_1, and $\boldsymbol{r} = x\hat{\boldsymbol{x}} + z\hat{\boldsymbol{z}}$ is a vector of components (x, z) in the Cartesian basis $(\hat{\boldsymbol{x}}, \hat{\boldsymbol{z}})$.

The surface current [$\psi(\boldsymbol{r})$ or $\partial\psi(\boldsymbol{r})/\partial n$] is computed by discretizing the integral equations from the MoM by using the point matching method with pulse basis functions. This leads to the linear system, $\bar{\boldsymbol{Z}}\boldsymbol{X} = \boldsymbol{b}$, where $\bar{\boldsymbol{Z}}$ is the impedance matrix, $\boldsymbol{X}$ is the unknown vector [of components $\partial\psi(\boldsymbol{r})/\partial n$ or $\psi(\boldsymbol{r})$ discretized on the surface], and $\boldsymbol{b}$ is the vector of the incidence field components discretized on the surface.

The scattered field in Ω_1 is then computed by applying Huygens' principle, leading $\forall \boldsymbol{r} \in \Omega_1$ to

$$\psi_{\text{sca}}(\boldsymbol{r}) = \int_S \left[\psi(\boldsymbol{r}') \frac{g(\boldsymbol{r}', \boldsymbol{r})}{\partial n} - \frac{\partial \psi(\boldsymbol{r}')}{\partial n} g(\boldsymbol{r}', \boldsymbol{r}) \right] dS'. \tag{3}$$

Depending on polarization, $\psi(\boldsymbol{r})$ or $\partial\psi(\boldsymbol{r})/\partial n$ is known from the BIE solution; the companion quantity in (3) is again determined using the IBC in (1).

B. Subdomain Decomposition Iterative Method

In [11] and [13], the FB [15], [16] was applied to solve the linear system $\bar{\boldsymbol{Z}}\boldsymbol{X} = \boldsymbol{b}$. The advantage of FB, of complexity $P_{\text{FB}}\mathcal{O}(N^2)$ (P_{FB} is the order of convergence), is that the impedance matrix $\bar{\boldsymbol{Z}}$ is not stored and then only a row of the impedance matrix needs to be stored. But, its main drawback is that this calculation is done for each order of the FB. To overcome this issue, the recent SDIM [14] is applied to solve the linear system.

SDIM consists in splitting the sea surface Σ into K subsurfaces Σ_i ($\Sigma = \Sigma_1 \cup \Sigma_2 \cup \ldots \cup \Sigma_K$). Then, it first computes the surface current on each isolated subsurface Σ_k ($\boldsymbol{X}_k$) and next, from an iterative scheme, it updates the current density by interacting the subdomains between them. Then

$$\boldsymbol{X} \approx \sum_{p=0}^{P=P_{\text{SDIM}}} \boldsymbol{Y}^{(p)} \tag{4}$$

where

$$\begin{cases} \boldsymbol{Y}_k^{(0)} = \bar{\boldsymbol{Z}}_{k,k}^{-1} \boldsymbol{v}_k \\ \boldsymbol{Y}_k^{(p)} = -\bar{\boldsymbol{Z}}_{k,k}^{-1} \displaystyle\sum_{n=1, n\neq k}^{K} \bar{\boldsymbol{Z}}_{n,k} \boldsymbol{Y}_n^{(p-1)} \quad p > 0 \end{cases} \tag{5}$$

where $\boldsymbol{Y}_k^{(p)}$ is the surface current at the order p on the subsurface k, $\boldsymbol{v}_k$ is the incident field on the subsurface k, and $\bar{\boldsymbol{Z}}_{n,k}$ the impedance matrix between the subsurface n and k (propagation of the scattered field from n toward k). The order of convergence P_{SDIM} is obtained from the criteria on relative residual error (RRE) defined by

$$\text{RRE} = \frac{\|\boldsymbol{X}^{(p)} - \boldsymbol{X}^{(p-1)}\|}{\|\boldsymbol{X}^{(p)}\|}. \tag{6}$$

Typically, the threshold of SDIM is chosen as $\epsilon_{\text{SDIM}} = 0.01$.

If the block matrices of $\bar{\boldsymbol{Z}}$ can be stored, their calculations are done at the beginning and then the complexity of SDIM is then

$$C_{\text{SDIM}}^{\text{ACA}} = K[\mathcal{O}(M^3) + P_{\text{SDIM}}(K-1)M^2(1-\bar{\tau}_{\text{ACA}})] \tag{7}$$

where M is the size of the block matrices assumed to be the same for all the blocks ($N = KM$). $\bar{\tau}_{\text{ACA}}$ is the mean compression ratio of ACA applied on the coupling matrices $\{\bar{\boldsymbol{Z}}_{n,k}\}$. If ACA is not applied, then $\bar{\tau}_{\text{ACA}} = 0$.

Moreover, with SDIM, the number of elements to store is

$$M_{\mathrm{SDIM}}^{\mathrm{ACA}} = KM^2[1 + (K-1)(1-\bar{\tau}_{\mathrm{ACA}})] \tag{8}$$

instead of $N^2 = K^2M^2$ to store $\bar{\bar{Z}}$. If $K \gg 1$, then, $M_{\mathrm{SDIM}} \approx N^2(1-\bar{\tau}_{\mathrm{ACA}})$, and the memory requirement is reduced by $1/(1-\bar{\tau}_{\mathrm{ACA}})$. Typically, if $\bar{\tau}_{\mathrm{SDIM}} = 0.99$, then, the reduction is of 100.

In addition, if the FBSA algorithm is applied to calculate the local interactions on each subsurface, the complexity and the memory requirement are $M\mathcal{O}(M_{\mathrm{FBSA}})$, where $M = N/K$ and $M_{\mathrm{FBSA}} \ll M$ instead of M^2 and $\mathcal{O}(M^2)$, respectively, from FB.

Then, combining SDIM + ACA with FBSA, (7) and (8) become

$$C_{\mathrm{SDIM}}^{\mathrm{ACA+FBSA}} = N[\mathcal{O}(M_{\mathrm{FBSA}})(1+P_{\mathrm{SDIM}}) + P_{\mathrm{SDIM}}M(K-1)(1-\bar{\tau}_{\mathrm{ACA}})] \tag{9}$$

and

$$M_{\mathrm{SDIM}}^{\mathrm{ACA+FBSA}} = N[\mathcal{O}(M_{\mathrm{FBSA}}) + M(K-1)(1-\bar{\tau}_{\mathrm{ACA}})]. \tag{10}$$

In conclusion, $C_{\mathrm{SDIM}}^{\mathrm{ACA+FBSA}}$ and $M_{\mathrm{SDIM}}^{\mathrm{ACA+FBSA}}$ are nearly proportional to N in terms of complexity and memory requirement, instead of $\mathcal{O}(N^3)$ and N^2, respectively, if a direct LU decomposition is applied on the matrix $\bar{\bar{Z}}$. These fundamental properties will allow us to solve rapidly huge propagation and scattering problems.

The principle of ACA compression is briefly summarized in [14]. A detailed explanation of SA can be found in [17] and [21].

III. Green Function

A. Case of a Refractive Index of Linear Profile

From [22], Bourlier and Pinel [18] evaluated the scalar Green's function for a homogeneous medium Ω_1 overlying a duct (medium Ω_2) with a linear-square refractive index profile (the rough surface was not considered), $n(z) = (1-\epsilon z)^{1/2} \approx 1 - \epsilon z/2$ with $|\epsilon z| \ll 1$. From the boundary conditions, the exact spectral Green's function is derived with the help of Airy functions. To have a closed-form expression of the corresponding spatial Green's function, the method of steepest descents is applied [22], leading to two terms. The first one corresponds to the Green function derived from the PWE approximation for an observation point $\boldsymbol{r}'$ far from the transmitter point $\boldsymbol{r}$ [paraxial approximation, $R = \|\boldsymbol{r}-\boldsymbol{r}'\| \approx X + (z'-z)^2/(2X)$ with $X = |x'-x|$, and the point $\boldsymbol{r}'$ is in far-field zone]. The second term is related to an evanescent wave (pole of Green's function), for which, its contribution can be neglected when the rough surface is accounted for [13]. In addition, to retrieve the exact Green function in free space, $g_0(\boldsymbol{r},\boldsymbol{r}') = (j/4)H_0^{(1)}(k_0\|\boldsymbol{r}-\boldsymbol{r}'\|)$ (where $H_0^{(1)}$ is the zeroth-order Hankel function of the first kind), from a heuristic way, the Green function is modified, such as $g = g_0$ for $\boldsymbol{r}' \to \boldsymbol{r}'$ (the refraction phenomenon can be neglected). Then, they showed for $n(z) = 1 - \epsilon z/2$ ($|\epsilon z| \ll 1$), that

$$g(\boldsymbol{r},\boldsymbol{r}') \approx g_0(\boldsymbol{r},\boldsymbol{r}')e^{-jk_0\left[\frac{\epsilon X(z+z')}{4}+\frac{\epsilon^2X^3}{96}\right]} \tag{11}$$

where $X = |x'-x|$.

B. Case of a Refractive Index of Any Profile

For any profile of the refractive index and under the PWE approximation, the spatial Green function is [9]

$$g(\boldsymbol{r},\boldsymbol{r}') = g_0^{\infty}(\boldsymbol{r},\boldsymbol{r}') \times \exp\left\{jk_0\left[\int_x^{x'} u(x_1)dx_1 - \frac{(z'-z)^2}{2X}\right]\right\} \tag{12}$$

where

$$u(x_1) = \frac{\gamma(x_1)^2}{2} + n(z(x_1)) - 1 \tag{13}$$

and $z(x_1)$ is the equation of the path ray to be determined. Its derivation is presented in Appendix A. The refractive index is assumed to be independent of the abscissa x_1. The elementary optical path length udx can be derived by writing that $udx = n((dx)^2+(dz)^2)^{1/2} = n(1+\gamma^2)^{1/2}|dx| \approx n(1+\gamma^2/2)|dx| \approx [1+(n-1)+\gamma^2/2]|dx|$ ($(n-1)\gamma^2/2$ is a term of order 2), where $\gamma = dz/dx$. Then, $(n-1+\gamma^2/2)|dx|$ stands for the deviation of the elementary optical path length from that of the free space.

To be consistent with (11), in (12), the term $-(z'-z)^2/(2X) = X - R$ (under the PWE approximation) is added. In (12), g_0^{∞} is the Green function in far field. Then, to retrieve the Green function in free space for $\boldsymbol{r}' \to \boldsymbol{r}'$, in (12), g_0^{∞} is substituted for g_0, leading to

$$g(\boldsymbol{r},\boldsymbol{r}') = \frac{j}{4}H_0^{(1)}(k_0\|\boldsymbol{r}-\boldsymbol{r}'\|) \times \exp\left\{jk_0\underbrace{\left[\int_x^{x'} u(x_1)dx_1 - \frac{(z'-z)^2}{2X}\right]}_{\delta}\right\}. \tag{14}$$

C. Case of a Refractive Index of Parabolic Profile

Appendix B presents the derivation of the Green function for a refractive index profile defined as

$$n(z) = 1 - \epsilon_1 z + \frac{\epsilon_2^2 z^2}{2}. \tag{15}$$

From (14) and (B3), the optical path length is

$$\delta(X,z,z') = \frac{\epsilon_1^2[\tanh(u)-u]}{\epsilon_2^3} - \frac{(z+z')\epsilon_1\tanh(u)}{\epsilon_2} + \frac{\epsilon_2(z'-z)^2}{2}\left[\coth(2u) - \frac{1}{2u}\right] + z'z\epsilon_2\tanh(u) \tag{16}$$

where $u = \epsilon_2 X/2 = \epsilon_2|x'-x|/2$. Appendix B also shows that the limit case of a linear refractive index profile, for which $\epsilon_2 = 0$, is retrieved.

IV. Numerical Results

For the simulations, it is assumed that the rough sea surface height is a stationary Gaussian stochastic process with zero mean value, and that the height spectrum obeys the Elfouhaily *et al.* [24] hydrodynamic spectrum, in which the key parameter is the wind speed u_{10} at 10 m above the sea surface.

A. Incident Field

The incident field, which appears in (2), is defined as the field produced by the source (antenna) that would exist in the duct in the absence of the rough surface. When the BIE approach is used to simulate the problem of propagation over a rough surface in a ducting medium, it is appropriate to calculate the field produced by the source, the initial field, $\psi_l^a(z_a)$, on a given vertical plane defined at $x = 0$. The incident field on the rough surface, $\psi_l(\boldsymbol{r})$ ($\boldsymbol{r} \in S$), is then evaluated by propagating the initial field from the vertical plane onto the rough surface using the ducting medium propagator.

For grazing angles ($\theta_l \to \pi/2$), Bourlier *et al.* [13] showed that this field can be approximated as [see (C5)]

$$\psi_l^a(z_a) \approx \exp\left(jk_0(z_a - z_{a,0})\cos\theta_l - \frac{(z_a - z_{a,0})^2}{g_z^2}\right) \quad (17)$$

where

θ_l	the look angle measured from the positive z-axis;
$\psi_l^a(z_a)$	the incident field on the surface S_a (z_a varies);
$z_{a,0}$	the center of the antenna (constant number) with respect to z (the abscissa of the antenna is set to zero);
g_z	the vertical footprint (in the plane $x = 0$).

From the knowledge of $\psi_l^a(z_a)$, Bourlier *et al.* [13] then showed that the propagated field in Ω_2 is

$$\psi_l(\boldsymbol{r}) \approx -2jk_0 \int_{S_a} \psi_l^a(\boldsymbol{r}_a) g_2(\boldsymbol{r}_a, \boldsymbol{r}) dz_a. \quad (18)$$

Equation (18) can be expressed as a vector-matrix product

$$\boldsymbol{b} = -8k_0 \bar{\boldsymbol{Z}}_{\mathrm{TE}}^{\boldsymbol{r}_a \to \boldsymbol{r}} \boldsymbol{b}_a \quad (19)$$

where $\bar{\boldsymbol{Z}}_{\mathrm{TE}}$ is the impedance matrix obtained from the Dirichlet boundary condition and $\boldsymbol{b}_a$ is the vector of components $\psi_l^a(z_a)$ discretized on the surface S_a.

From (3), the scattered field can also be expressed as a vector matrix product

$$\boldsymbol{b}_{\mathrm{sca}} = -\bar{\boldsymbol{Z}}_{\mathrm{TE,TM}}^{\boldsymbol{r} \to \boldsymbol{r}'} \boldsymbol{X} \quad (20)$$

where $\bar{\boldsymbol{Z}}_{\mathrm{TE,TM}}^{\boldsymbol{r} \to \boldsymbol{r}'}$ is the impedance matrix obtained from the IBC boundary condition and for the TE and TM polarizations, respectively.

For a huge problem, the numerical computation of integrals (3) and (18) are very time consuming. Thus, to overcome this issue, the ACA algorithm can also be applied to compute the integrals from the matrix forms (19) and (20).

First, numerical results of SDIM at level 1, presented in Section II, are shown. The simulation parameters are reported in the second column of Table I. The subscript "1" refers to the variables defined at level 1. Next, to treat huge problems, numerical results of SDIM at level 2 are shown. The simulation parameters are reported in the third column of Table I. The subscript "2" refers to the variables defined at level 2. This means in (5) that the SDIM is applied again for the calculation of the vector-matrix product $\bar{\boldsymbol{Z}}_{k,k}^{-1} \boldsymbol{v}_k$.

TABLE I

SIMULATION PARAMETERS. THE DUCT PARAMETERS ϵ_1 AND ϵ_2 ARE OBTAINED FROM n_0 AND n_c AS $\epsilon_1 = 2(n_0 - n_c)/z_c$ AND $\epsilon_2 = (2(n_0 - n_c))^{1/2}/z_c$. THE HEIGHT z_c IS DEFINED AS $n'(z_c) = 0$. THE SURFACE SAMPLING STEP IS $\Delta x = \lambda_0/8$. THE SECOND COLUMN (SDIM AT LEVEL 1, SUBSCRIPT "1") IS FOR FIGS. 3–7. THE THIRD COLUMN (SDIM AT LEVEL 2, SUBSCRIPT "2") IS FOR FIGS. 8 AND 9

Duct parameter $n(0) = n_0$	1.03	1.003
Duct parameter $n(z_c) = n_c$	1	1
Duct parameter z_c [m]	20	20
Wavelength λ_0 [m]	0.1	0.1
Incidence angle θ_l [°]	88	89
Polarization	TE	TE
Vertical footprint g_z [m]	3	3
Transmitter center $z_{a,0}$ [m]	10	10
Transmitter heights z_a [m]	$z_a \in [7; 13]$	$z_a \in [7; 13]$
Sea permittivity ϵ_{r3}	$70.4 + 40.6j$	$70.4 + 40.6j$
Surface length L [m]	375	1250
Wind speed u_{10} [m/s]	5	10
Number of unknowns N	30,000	100,000
Numbers of blocks (K_1, K_2)	(10,-)	(5,10)
Threshold of ACA ϵ_{ACA}	0.001	0.001
Threshold of FB ϵ_{FB}	0.01	0.01
Thresholds of SDIM $(\epsilon_{1,\mathrm{SDIM}}, \epsilon_{2,\mathrm{SDIM}})$	(0.01,-)	(0.01,0.01)
Overlapping $(n_{1,\mathrm{OL}}, n_{2,\mathrm{OL}})$	(20,-)	(20,20)

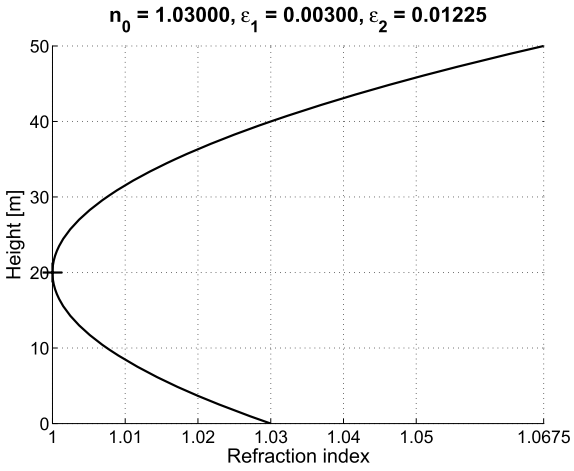

Fig. 2. Height versus the refractive index.

B. SDIM at Level 1

First, a small problem of $N = 30\,000$ unknowns is considered. The simulation parameters are reported in Table I.

The parabolic profile of the refractive index, $n(z)$, is plotted in Fig. 2 versus the height z. As we can see for $z \in [0; z_c = \epsilon_1/\epsilon_2^2]$ ($n'(z_c) = 0$), the gradient of $n(z)$ is negative, whereas for $z > z_c$, it is positive. The use of a parabolic profile allows us to consider jointly a positive and negative gradient, which is not possible from a linear profile.

1) Comparison of SDIM + LU and SDIM + LU + ACA With LU: Fig. 3 plots the modulus of the surface currents versus the surface abscissa. The labels in the legend mean the following:

1) "LU" stands for the surface currents computed from a direct LU inversion by considering only one block (brute force of MoM).

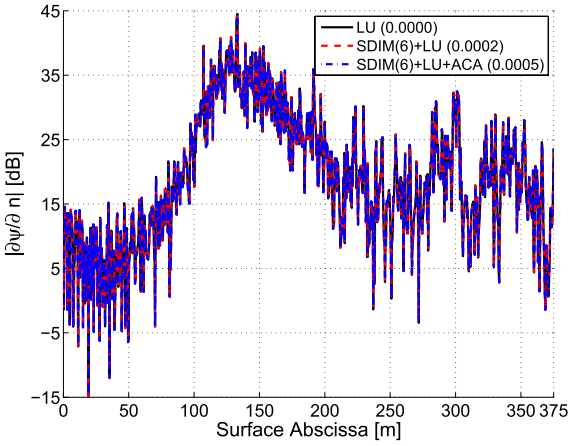

Fig. 3. Modulus of the surface currents versus the surface abscissa. The order P of SDIM changes.

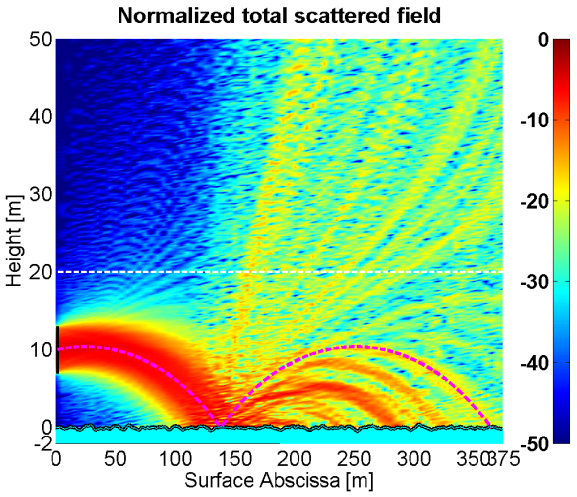

Fig. 4. Modulus of the total field normalized by its maximum computed from "LU" and on the grid (x_0, z_0) with $x_0 \in [0; L = 375]$ m and $z_0 \in [0; 50]$ m.

2) "SDIM(P_{SDIM}) + LU" stands for the surface currents computed from a direct LU inversion for each subblock, and P_{SDIM} is the convergence order of SDIM. In addition, the value between parenthesis is the RRE between the surface currents at the order P_{SDIM} and that computed from 'LU."
3) "SDIM(P_{SDIM}) + LU + ACA" stands for the surface currents computed from a direct LU inversion for each subblock when the ACA algorithm is applied for the coupling steps between the subsurfaces. In addition, the value between parenthesis is the RRE between the surface currents at the order P_{SDIM} and that computed from 'LU." The ACA threshold is $\epsilon_{\text{ACA}} = 10^{-3}$.

As we can see, SDIM converges rapidly and the RRE does not exceed the SDIM threshold $\epsilon_{1,\text{SDIM}}$ set to 10^{-2}. Simulations, not reported in this paper, showed that $\epsilon_{1,\text{SDIM}}$ can be set to 5×10^{-2} and then $P_{\text{SDIM}} = 5$. In addition, Fig. 3 shows that the use of ACA, with a threshold equals $\epsilon_{\text{ACA}} = 10^{-3}$, does not degrade the results. The mean compression ratio of ACA is $\bar{\tau}_{\text{ACA}} = 0.9923$ and $\bar{\tau}_{\text{ACA}} \in [0.9781; 0.9967]$, which shows that ACA is very efficient.

Fig. 4 plots the modulus of the total field normalized by its maximum computed from "LU" and on the grid (x_0, z_0) with $x_0 \in [0; L]$ and $z_0 \in [0; 50]$ m. At $x = 0$, the thick vertical line shows the extension of the source (antenna). The horizontal dashed curve plots the height $z_c = 20$ m and the dashed curve plots the ray trajectory calculated for an initial point of coordinates $(0, z_{a,0})$ and of initial slope $\cot\theta_l$. Appendix C gives the mathematical expression of the ray trajectory and these properties (maximum, roots).

Before the first bounce defined at the abscissa $x = X_2 \approx 138$ m [obtained by (C4)], the main contribution is given by the incident field. The incident field is trapped in the duct defined for $z \in [0; z_c]$, because the height of the antenna does not exceed a critical height $z_{a,c}$, for which the ray leaves the duct. From Appendix C, it is defined as

$$z_{a,c} = z_c - \frac{\cot\theta_l}{\epsilon_2} \tag{21}$$

and equals $z_{a,c} = 17.11$ m $> \max(z_a) = 13$ m.

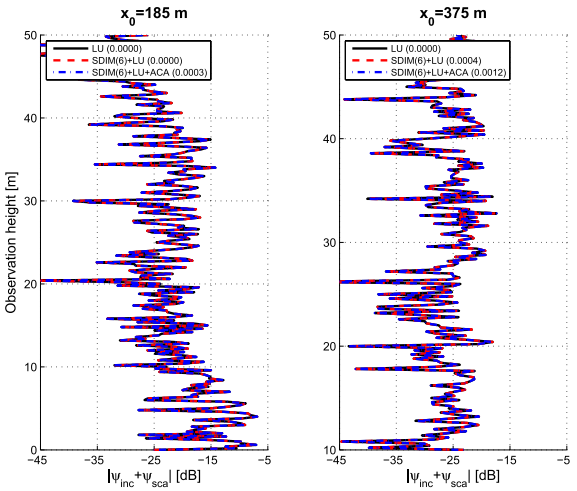

Fig. 5. Modulus of the normalized total field versus the height z_0 and for given $x_0 = \{185, 375\}$ m.

Unlike the incident field, a part of the scattered field radiated by the surface currents produced by the first bounce is not trapped and can leave the duct (defined for $z \in [0; z_c]$). Due to the surface roughness, the angles of the first bounces $\theta_{r,1}$ are defined around $\bar{\theta}_{r,1} \approx 78^o$ [case of a flat surface defined from (C6)]. From (21), if $\theta_{r,1} < \text{acot}(\epsilon_2 z_c) = 76.4^o$ ($z_{a,c} = 0$), then the corresponding ray leaves the duct, which explains the behavior of the total field in the region $z_0 > z_c$. In addition, for this region, the ray trajectories are convex, because the gradient of the refractive index is positive. For a linear refractive index profile, this effect cannot occur because the gradient is always negative for any height.

Fig. 5 plots the modulus of the normalized total field versus the height z_0 and for the given abscissa $x_0 = \{185, 375\}$ m. As we can see, the curves perfectly match, which shows that the threshold of SDIM is well chosen. In the legend, the number within parenthesis gives the value of the RRE [see (6)] defined for the total field and computed for each x_0.

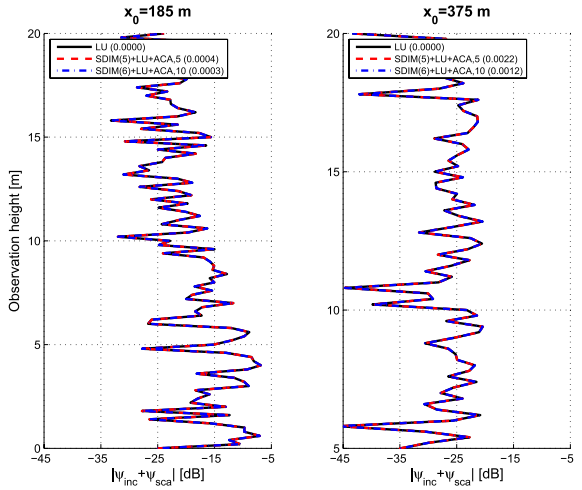

Fig. 6. Similar variation as in Fig. 5 but the number of blocks $K_1 = \{5, 10\}$ changes.

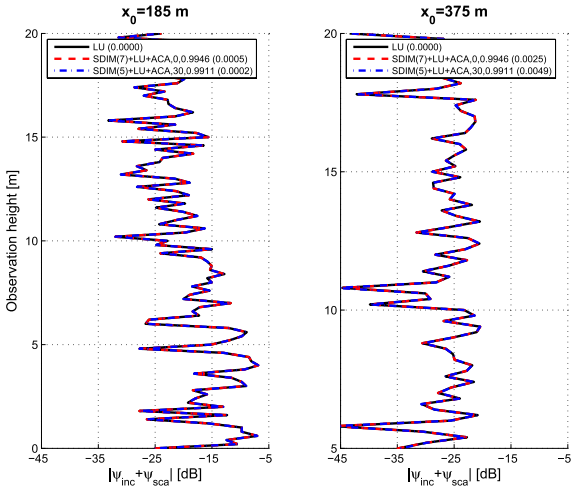

Fig. 7. Similar variations as in Fig. 5, in which SDIM + LU + ACA is tested versus $n_{1,\mathrm{OL}} = \{0, 30\}$.

From (20), the scattered field computed on the grid of observation (x_0, z_0) is calculated from ACA to accelerate the calculation of the numerical integration. The complexity of ACA is $\mathcal{O}(R^2(N_1 + N_2))$, where $R \ll (N_1, N_2)$ is the effective rank of the matrix to compress, $\bar{\bar{A}}$, and (N_1, N_2) its sizes. Numerical trials showed, for compressions ratio smaller than 0.7, that the computing time to calculate $\bar{\bar{A}}$ can be larger than that to calculate $\bar{\bar{A}}$ without compression. It comes from R^2 in the complexity. Physically, the compression ratio can be small for two vertical close plates located face to face, because the coupling is strong. Then, some points of the plates are sufficient to degrade the compression. To improve the compression for the radiation of the surface currents, the sea surface is then split up into K subsurfaces of the number of samples M_i ($\sum_{i=1}^{K} M_i = N$), like SDIM. In addition, for $x_0 \in [x_i; x_{i+1}]$, where $[x_i; x_{i+1}]$ is the range of the abscissa of the subsurface i, the ACA algorithm is not applied, since z_0 can be close to the height of the subsurface i, implying that ACA is not efficient. In the following $K = M$.

For instance, in Fig. 5, for $x_0 = \{185, 375\}$, the mean compression ratio is of the order of 0.85 and ACA is not efficient for two subblocks on 10.

From (19), the incident field on the surface is also calculated from ACA (to accelerate the calculation of the numerical integration). The resulting mean compression ratio is then 0.969, which shows that ACA is very efficient.

2) SDIM + LU + ACA Versus the Number of Blocks K_1: Fig. 6 plots the same variation, as in Fig. 5, but the number of blocks $K_1 = \{5, 10\}$ changes. In the label, the integer after the comma is the number of blocks K_1. As we can see, as K_1 increases, the SDIM convergence order P_{SDIM} increases one order of magnitude (from 5 to 6), because more iterations are needed to account for the coupling between smaller subsurfaces. In addition, as K_1 increases, the RRE slightly increases. For $K_1 = 15$ (not shown here), $P_{\mathrm{SDIM}} = 6$ (as for $K_1 = 10$) and the RRE equals 0.0058 for $x_0 = 375$ m in Fig. 6. For $K_1 = 20$, SDIM does not converge because the sizes of the blocks, which equal to $30\,000/20 = 1500$, are too small.

3) Overlapping Between the Adjacent Subblocks: A means to reduce the number of iterations of SDIM is to overlap the adjacent subsurfaces of a few tens of samples ($n_{1,\mathrm{OL}}$), to decrease the contribution of the edges diffraction coming from the finiteness of the subsurfaces.

Fig. 7 plots the same variations, as in Fig. 5, in which SDIM + LU + ACA is tested versus $n_{1,\mathrm{OL}} = \{0, 30\}$. In the legend, the integer after the comma is $n_{1,\mathrm{OL}}$, and the next number, the mean compression ratio of ACA $\bar{\tau}_{\mathrm{ACA}}$. As $n_{1,\mathrm{OL}}$ increases, P_{SDIM} slightly decreases without loss in precision. On the other hand, as $n_{1,\mathrm{OL}}$ increases, $\bar{\tau}_{\mathrm{ACA}}$ slightly decreases, meaning that the ACA compression is less efficient, because the overlapping of the adjacent subsurfaces implies a strong local interaction between the $n_{1,\mathrm{OL}}$ common points. For $n_{1,\mathrm{OL}} = 20$, P_{SDIM} is the same as that obtained for $n_{1,\mathrm{OL}} = 30$.

4) Comparison of SDIM + FB + ACA With LU: The label "SDIM + FB + ACA" means that the surface currents are computed from FB (instead from a direct LU inversion) for each subblock and the ACA algorithm is applied for the coupling steps between the subsurfaces. The results, not depicted here, showed that the surface currents and the associated scattered field perfectly match with those obtained from "LU." Then, a threshold of FB of 0.01 is a good choice. Typically, the convergence order of FB is from 4 to 5 for the TE polarization and from 2 to 3 for the TM case.

5) TM Polarization: Same simulations were done for the TM polarization. In comparison to the TE polarization, the results, not depicted here, showed that SDIM converges more rapidly (4 instead of 6), is less sensitive to the number of blocks K_1 and is nearly independent of $n_{1,\mathrm{OL}}$. This conclusion is the same as that drawn in [14] for airborne applications.

C. SDIM at Level 2

The section IV-B showed that if the number of blocks K_1 is too large, the SDIM can fail. It is the first condition. On the other hand, to apply the FBSA, the subdomains must be homogeneous, which means that the number of

samples M_1 ($N_1 = K_1 M_1$) per block must not be too large, or in other words, K_1 must be large enough. This second condition is in contradiction with the first one. Then, to satisfy condition 1, the subsurface lengths of level 1 are large enough, whereas to satisfy condition 2, the subsurfaces lengths of level 2 (each subsurface of level 1 is split up into K_2 subsurfaces of level 2) are small enough to apply the FBSA. Level 2 means in (5) that the SDIM is applied again for the calculation of the vector-matrix product $\bar{\boldsymbol{Z}}_{k,k}^{-1}\boldsymbol{v}_k$.

To estimate the maximum length $X_{\max}$ of the subsurfaces of level 2, an upper bound, $\delta_{\max}$, of the optical path length δ, expressed from (16) and which appears in the Green function (14), must be found. Assuming that $u = \epsilon_2 X/2$ is close to zero and making a series expansion of u around zero, we show from (16) that

$$\delta_{\max} \approx \left(\frac{\hat{\sigma}_z \epsilon_1 \epsilon_2^2}{12} + \frac{\epsilon_1^2}{24} + \frac{31\hat{\sigma}_z^2\epsilon_2^4}{360}\right) X^3 + \hat{\sigma}_z \left(\epsilon_1 + \frac{7\hat{\sigma}_z \epsilon_2^2}{6}\right) X \tag{22}$$

where $\max(z + z') \approx 2\hat{\sigma}$, $\max((z - z')^2) \approx 4\hat{\sigma}_z^2$, $\max(zz') \approx \hat{\sigma}_z^2$, and $\hat{\sigma}_z$ is of the order of the surface height standard deviation σ_z. Typically, $\hat{\sigma}_z = 2\sigma_z$.

Then, each subdomain of level 2 can be considered as homogeneous if $\delta_{\max}$ does not exceed the threshold value δ_0. Typically, $\delta_0 = \lambda_0/8$ is a fraction of the wavelength λ_0. Imposing that $\delta_{\max} = \delta_0$, from (22), $X_{\max} = X$ is computed by solving an equation of third degree on X.

The simulation parameters are reported in the third column of Table I.

1) Comparison of SDIM + LU + ACA With SDIM + FB0 + ACA: Before comparing SDIM + FBSA + ACA (FBSA is used to calculate the local interactions on each subsurface) with SDIM + LU + ACA, SDIM + FB0 + ACA (FB0 is used to calculate the local interactions on each subsurface, where the label "0" means that the Green function in free space is applied) is compared with SDIM + LU + ACA in order to study the impact of the numbers of blocks K_1 and K_2. Indeed, the choices of K_1 and K_2 are governed by the fact that the lengths of the subsurfaces of level 2 are small enough to use the Green function in free space to compute the local interactions on each subsurface.

Figs. 8 and 9 plot the modulus of the normalized total field versus the height z_0, for given $x_0 = \{620, 1275\}$ and for the TE and TM polarizations, respectively. In the legends, the numbers are $P_{1,\mathrm{SDIM}}$ (SDIM convergence order at level 1), $\bar{P}_{2,\mathrm{SDIM}}$ (SDIM mean convergence order at level 2), K_1, K_2, and RRE, respectively. For $u_{10} = 10$ m/s, $X_{\max} \approx 40$ m, which implies that $\max(M_2) \approx 3164$. This corresponds to $K_1 = 4$ and $K_2 = 8$ ($N = 100\,000/(4 \times 8) = 3125$). Figs. 8 and 9 then showed for $(K_1, K_2) = (4, 8)$, the results match well with those obtained from "SDIM + LU + ACA" and for $(K_1, K_2) = (5, 5)$, the difference slightly increases, because the lengths of the subsurfaces at level 2 are too large to consider the local media as homogeneous.

2) Comparison of SDIM + LU + ACA With SDIM + FBSA + ACA: For the SA, the distance of the strong interaction, x_{strong}, must be determined. For airborne applications,

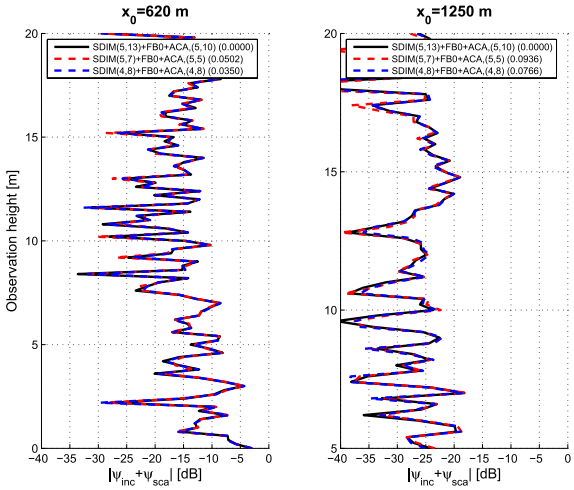

Fig. 8. Modulus of the normalized total field versus the height z_0 and for given $x_0 = \{620, 1275\}$ m. The polarization is TE.

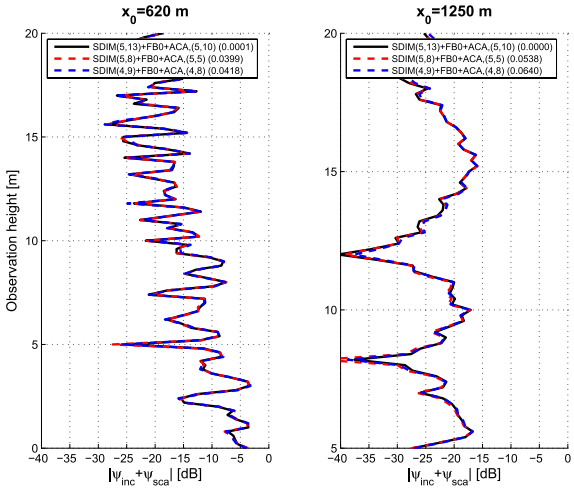

Fig. 9. Similar variation as in Fig. 8 but for the TM polarization.

Kubické *et al.* [25] showed that $x_{\mathrm{strong}} \approx 0.154\alpha u_{10}^2$, where $\alpha = 0.03$. For our application, we find that $\alpha \approx 0.6$, which shows that x_{strong} is larger than that used for a propagation in free space and in far field. The simulation parameters are $z_c = 30$ m, $f = 5$ GHz, $\theta_l = 89.9°$, $n_0 = 1.0002$, and $K_1 = K_2 = 5$ and the other parameters are unchanged (third column of Table I). The number of unknowns is then $N = 400\,000$ (surface length equals 3000 m), which is the upper limit (in memory space, the MATLAB software is used for the simulations and the computer configuration is IntelXeon, 2.67 GHz, two processors, 192 GB) that my PC can solve from SDIM + LU + ACA.

Figs. 10 and 11 plot the normalized total field versus the height z_0, for the given $x_0 = \{1500, 3000\}$ and for the TE and TM polarizations, respectively. In the legend, for the FBSA, the integer 308 is the number of samples of the strong interactions (integer part of $x_{\mathrm{strong}}/\Delta x$, where $\Delta x = \lambda_0/8$). The number of samples per block is $M = 16\,000$. As we can see, good agreement between SDIM + FBSA + ACA and SDIM + LU + ACA is obtained, which shows that the distance x_{strong} and the number of subblocks $K_1 K_2 = 25$

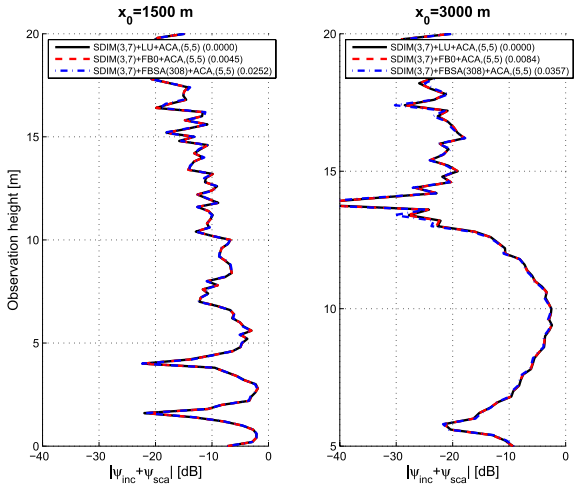

Fig. 10. Modulus of the normalized total field versus the height z_0 and for given $x_0 = \{1500, 3000\}$ m. The polarization is TE.

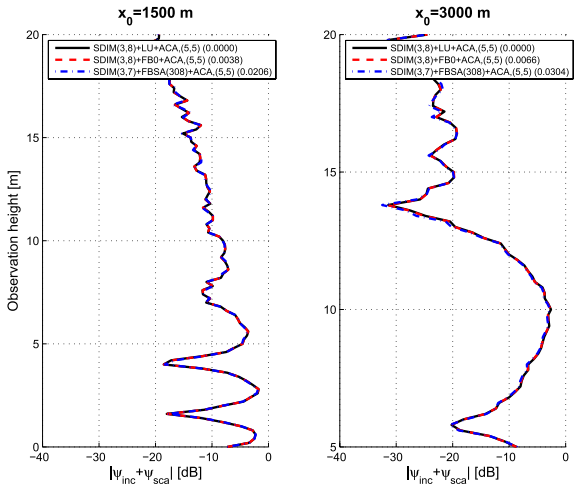

Fig. 11. Same variation as in Fig. 10 but for the TM polarization.

are well chosen. The results obtained from SDIM + FB0 + ACA are better, because SA is not applied.

We can note that the mean compression ratios at levels 1, $\bar{\tau}_{1,\mathrm{ACA}}$, and 2, $\bar{\tau}_{2,\mathrm{ACA}}$, range from $\bar{\tau}_{1,\mathrm{ACA}} \in [0.9984; 0.9998]$ ($M_1 = 20\,000$) and $\bar{\tau}_{2,\mathrm{ACA}} \in [0.9849; 0.0.9984]$ ($M_2 = M_1/5 = 4000$), respectively, with mean values 0.9995 and 0.9957, respectively. As expected, as the sizes of the coupling matrices increase, the compression ratio of ACA tends toward 1. Then, the efficiency of the proposed method increases as the surface length increases.

V. Conclusion

In this paper, the BIE subdomain iterative method (SDIM) combined with ACA and FBSA was employed to enhance the numerical efficiency of the SDIM for propagation over finitely conducting surfaces. The combined SDIM/FBSA scheme substantially expedited the costly matrix-vector operation needed in the iterative FB procedure for calculating the surface currents on each subsurface. In the same way, the ACA scheme substantially speeds up the costly matrix-vector operation required for coupling steps between the subsurfaces.

Being a BIE scheme, the SDIM + ACA + FBSA procedure incorporates the multiscale of the ocean surface in a rigorous manner. This capability avoids the use of approximate coherent models for reflection from the rough sea surface applied in the PWE-SSF scheme. The proposed method accounts for ducting conditions by using the PWE for the derivation of the Green function, hence preserving some of the attractive features of the PWE-SSF scheme. For the time being, the SDIM is meant to be a companion and not an alternative to the more efficient PWE-SSF approach.

To apply the FBSA, each subblock must be considered as homogeneous, which imposes a maximum size. Then, the SDIM has been extended to two levels to treat large surfaces. The refraction phenomenon is accounted for the coupling matrices between the subblocks. A parabolic refractive index profile is considered in this paper, but since the block sizes are small, the derivation of the Green function can be generalized to any profile by making a series expansion of $u(x_1)$ [defined from (13)] over $X_1 = x_1 - x$.

To enhance the numerical efficiency of SDIM, a parallelization can be done. Indeed, the precomputations of impedance matrices $\bar{\boldsymbol{Z}}_{k,k}$ and $\bar{\boldsymbol{Z}}_{n,k}$ can be done in parallel and for a given order p of SDIM, the surface currents $\boldsymbol{Y}_k^{(p)}$ of each subsurface k can also be computed in parallel. To reduce again the complexity, expressed from (9), as shown in [14], the "weak coupling approximation" can be applied between the subblocks. This means in (5) that the index n ranges from $n-n_-$ to $n+n_+$ [with $\min(n) = 1$ and $\max(n) = K$] instead of $n \in [1; K]$ with $n \neq k$. For instance, if $n_- = 0$ and $n_+ = 1$, then, only the coupling between the current subblock n and the next one defined on the right is accounted for, which means that only the forward contribution is considered on the current subblock.

Appendix A
Equation of the Ray Path

This section presents the derivation of the equation of the path ray.

From the Snell–Descartes law, $n(z)\cos\alpha = \text{constant}$, where α is the angle defined with respect to the horizontal axis x. Deriving this equation with respect to x, one shows

$$\frac{d\cos\alpha}{dx} n(z) + \cos\alpha \frac{dn}{dx} = 0. \tag{A1}$$

Since $\tan\alpha = dz/dx$, one shows

$$-\sin\alpha \frac{n(z)}{1+\gamma^2(x)} \gamma'(x) + \cos\alpha \frac{dn}{dx} = 0 \tag{A2}$$

where $d\cos\alpha/dx = -\gamma'\sin\alpha/(1+\gamma^2)$, in which $\gamma' = d\gamma/dx = d^2z/dx^2$. The division in (A2) by $\cos\alpha$ leads to

$$-\frac{n(z)}{1+\gamma^2(x)} \gamma'(x) + \frac{dn}{dz} = 0 \tag{A3}$$

where $\sin\alpha/\cos\alpha = dz/dx$ and $dn/dx = (dn/dz)(dz/dx)$. The use of the paraxial approximation leads to $1 + \gamma^2(x) \approx 1$ and since $n(z)$ is a slow function with z, $(dn/dz)/n(z) \approx dn/dz$. Then, the equation of the ray

trajectory, $z(x)$, is derived by solving the following differential equation:

$$\frac{d^2z}{dx^2} = \frac{dn}{dz}. \tag{A4}$$

The derivation of $z(x)$ requires two integrations and then two constants are introduced. To calculate them, we impose $z(x) = z$ and $z(x') = z'$ [or $z(0) = z$ and $z(X) = z'$ with $X = x' - x$].

Appendix B
Case of a Refraction Index of Parabola Profile

This section presents the derivation of the Green function for the case of the parabolic refraction index profile defined by (15).

From (A4), we can show that ($dn/dz = \epsilon_1 - \epsilon_2 z$)

$$z(x) = \alpha e^{\epsilon_2 x} + \beta e^{-\epsilon_2 x} + \frac{\epsilon_1}{\epsilon_2^2}. \tag{B1}$$

The constants α and β are determined by imposing that $z(0) = z$ and $z(X) = z'$ ($X = x' - x$) leading to

$$\begin{cases} \alpha = -\dfrac{\epsilon_1}{(e^{\epsilon_2 X}+1)\epsilon_2^2} + \dfrac{z'e^{\epsilon_2 X} - z}{e^{2\epsilon_2 X} - 1} \\ \beta = -\dfrac{\epsilon_1 e^{\epsilon_2 X}}{(e^{\epsilon_2 X}+1)\epsilon_2^2} + \dfrac{e^{\epsilon_2 X}(ze^{\epsilon_2 X} - z')}{e^{2\epsilon_2 X} - 1}. \end{cases} \tag{B2}$$

The substitution of (B1) and (15) into (13) then leads to

$$u(x_1) = \epsilon_2^2(\alpha^2 e^{2\epsilon_2 x_1} + \beta^2 e^{-2\epsilon_2 x_1}) - \frac{\epsilon_1^2}{2\epsilon_2^2}. \tag{B3}$$

Then

$$\begin{aligned} \delta = {} & \frac{\epsilon_1^2[\tanh(u) - u]}{\epsilon_2^3} - \frac{(z + z')\epsilon_1 \tanh(u)}{\epsilon_2} \\ & + \frac{\epsilon_2(z' - z)^2}{2}\left[\coth(2u) - \frac{1}{2u}\right] \\ & + z'z\epsilon_2 \tanh(u) \end{aligned} \tag{B4}$$

where $u = \epsilon_2 X/2$.

For $\epsilon_2 \to 0$, $u \to 0$, $\tanh(u) \to u - u^3/3$, and $\coth(u) \to 1/u$. Then, the limit case, for which $\epsilon_2 = 0$, corresponding to a linear refractive index profile, (B4) becomes

$$\delta = -\frac{\epsilon_1^2 X^3}{24} - \frac{\epsilon_1 X(z' + z)}{2} + \frac{(z - z')^2}{2X}. \tag{B5}$$

Comparing (11) with (12), the phase term is then retrieved with $\epsilon_1 = \epsilon/2$.

Appendix C
Equation of the Ray Trajectory

From (A4), we can show that the equation of the ray trajectory is

$$z(X) = \epsilon_1 \frac{1 - \cosh(\upsilon)}{\upsilon^2} X^2 + \cot\theta_l \frac{\sinh(\upsilon)}{\upsilon} X + z_0 \cosh(\upsilon) \tag{C1}$$

where $z(0) = z_0$, $z'(0) = \cot\theta_l$, and $\upsilon = \epsilon_2 X = 2u$.

The abscissa for which $z'(X) = 0$ (extrema) is

$$X_E = \frac{\ln W}{2\epsilon_2} \quad W = \frac{\epsilon_2(z_c - z_0) + \cot\theta_l}{\epsilon_2(z_c - z_0) - \cot\theta_l} \tag{C2}$$

and the corresponding height $z(X_E)$ is

$$z_E = z_c - \frac{\sqrt{\epsilon_2^2(z_c - z_0)^2 - \cot^2\theta_l}}{\epsilon_2}. \tag{C3}$$

X_E is a real number if $W > 0$, implying that $z_0 < z_c - \cot\theta_l/\epsilon_2$.

The abscissa for which $z(X) = 0$ is

$$X_i = \frac{\ln W_i}{\epsilon_2} \tag{C4}$$

where

$$W_{1,2} = \frac{z_c\epsilon_2 \mp \sqrt{\epsilon_2^2(2z_c z_0 - z_0^2) + \cot^2\theta_l}}{\epsilon_2(z_c - z_0) - \cot\theta_l}. \tag{C5}$$

In addition, the angles θ_i defined at X_i are

$$\cot\theta_i = \sqrt{\epsilon_2^2(2z_c z_0 - z_0^2) + \cot^2\theta_l}. \tag{C6}$$

References

[1] M. Levy, *Parabolic Equation Methods for Electromagnetic Wave Propagation* (Electromagnetic Waves series 45). London, U.K.: The Institution of Electrical Engineers, 2000.

[2] W. S. Ament, "Toward a theory of reflection by a rough surface," *Proc. IRE*, vol. 41, no. 1, pp. 142–146, 1953.

[3] V. Fabbro, C. Bourlier, and P. F. Combes, "Forward propagation modeling above Gaussian rough surfaces by the parabolic shadowing effect," *Progr. Electromagn. Res.*, vol. 58, pp. 243–269, 2006.

[4] R. F. Harrington, *Field Computation by Moment Methods*. New York, NY, USA: Macmillan, 1968.

[5] L. Tsang, J. A. Kong, K.-H. Ding, and C. O. Ao, *Scattering of Electromagnetic Waves: Numerical Simulations* (Wiley Series on Remote Sensing), vol. 2. Hoboken, NJ, USA: Wiley, 2001.

[6] C. Bourlier, N. Pinel, and G. Kubické, *Method of Moments for 2D Scattering Problems: Basic Concepts and Applications* (FOCUS Wave Series). Hoboken, NJ, USA: Wiley, 2013.

[7] A. J. Robins, "Exact solutions of the Helmholtz equation for plane wave propagation in a medium with variable density and sound speed," *J. Acoust. Soc. Amer.*, vol. 93, no. 3, pp. 1347–1352, 1993.

[8] L. M. Brekhovskikh, *Waves in Layered Media*, 2nd ed. New York, NY, USA: Academic, 1980.

[9] B. J. Uscinski, "Sound propagation with a linear sound-speed profile over a rough surface," *J. Acoust. Soc. Amer.*, vol. 94, no. 1, pp. 491–498, 1993.

[10] R. S. Awadallah, "Rough surface scattering and propagation over rough terrain in ducting environments," Ph.D. dissertation, Dept. Elect. Eng., Virginia Polytech. Inst. State Univ., 1998.

[11] R. S. Awadallah and G. S. Brown, "Low-grazing angle scattering from rough surfaces in a duct formed by a linear-square refractive index profile," *IEEE Trans. Antennas Propag.*, vol. 48, no. 5, pp. 1461–1474, Sep. 2000.

[12] R. S. Awadallah, M. T. Lamar, and J. R. Kuttler, "An accelerated boundary integral equation scheme for propagation over the ocean surface," *Radio Sci.*, vol. 37, no. 5, pp. 8-1–8-16, 2002.

[13] C. Bourlier, H. Li, and N. Pinel, "Low-grazing angle propagation and scattering above the sea surface in the presence of a duct jointly solved by boundary integral equations," *IEEE Trans. Antennas Propag.*, vol. 63, no. 2, pp. 667–677, Feb. 2015.

[14] C. Bourlier, S. Bellez, H. Li, and G. Kubické, "Sub-domain decomposition iterative method combined with ACA: An efficient technique for the scattering from a large highly conducting rough sea surface," *IEEE Trans. Antennas Propag.*, vol. 63, no. 2, pp. 659–666, Feb. 2015.

[15] D. Holliday, L. L. DeRaad, Jr., and G. J. St-Cyr, "Forward-backward: A new method for computing low-grazing angle scattering," *IEEE Trans. Antennas Propag.*, vol. 44, no. 5, pp. 722–729, May 1995.

[16] D. A. Kapp and G. S. Brown, "A new numerical method for rough-surface scattering calculations," *IEEE Trans. Antennas Propag.*, vol. 44, no. 5, pp. 711–721, May 1996.
[17] H.-T. Chou and J. T. Johnson, "A novel acceleration algorithm for the computation of scattering from rough surfaces with the forward-backward method," *Radio Sci.*, vol. 33, no. 5, pp. 1277–1287, Sep./Oct. 1998.
[18] C. Bourlier and N. Pinel, "Spatial green function of a constant medium overlying a duct with linear-square refractive index profile," *IEEE Trans. Antennas Propag.*, vol. 61, no. 6, pp. 3172–3181, Jun. 2013.
[19] M. Bebendorf, "Approximation of boundary element matrices," *Numer. Math.*, vol. 86, no. 4, pp. 565–589, 2000.
[20] K. Zhao, M. N. Vouvakis, and J.-F. Lee, "The adaptive cross approximation algorithm for accelerated method of moments computations of EMC problems," *IEEE Trans. Electromagn. Compat.*, vol. 47, no. 4, pp. 763–773, Nov. 2005.
[21] C. Bourlier, G. Kubické, and N. Déchamps, "Fast method to compute scattering by a buried object under a randomly rough surface: PILE combined with FB-SA," *J. Opt. Soc. Amer. A*, vol. 25, no. 4, pp. 891–902, 2008.
[22] V. A. Fock, *Electromagnetic Diffraction and Propagation Problems*. Paris, France: Pergamon, 1965.
[23] E. I. Thorsos, "The validity of the Kirchhoff approximation for rough surface scattering using a Gaussian roughness spectrum," *J. Acoust. Soc. Amer.*, vol. 83, no. 1, pp. 78–92, 1988.
[24] T. Elfouhaily, B. Chapron, K. Katsaros, and D. Vandermark, "A unified directional spectrum for long and short wind-driven waves," *J. Geophys. Res.*, vol. 102, no. C7, pp. 15781–15796, 1997.
[25] G. Kubické, C. Bourlier, and J. Saillard, "Scattering from canonical objects above a sea-like one-dimensional rough surface from a rigorous fast method," *Waves Random Complex Media*, vol. 20, no. 1, pp. 156–178, 2010.

Christophe Bourlier was born in La Flèche, France, in 1971. He received the M.S. degree in electronics from the University of Rennes, Rennes, France, in 1995, and the Ph.D. degree from the Système Électronique et Informatique Laboratory, Nantes, France, in 1999.

He is currently with the Institute of Electronics and Telecommunications of Rennes Laboratory, University of Nantes, Nantes, France. He is a Researcher of the National Center for Scientific Research on electromagnetic wave scattering from rough surfaces (ocean like-surfaces) and objects for microwaves and infrared remote sensing applications and radar signatures. He has authored over 180 journal articles and conference papers.